Available online at www.sciencedirect.com

ScienceDirect

Geochimica et Cosmochimica Acta 293 (2021) 224–239

Geochimica et Cosmochimica Acta

www.elsevier.com/locate/gca

# Predicting nitrogen and oxygen kinetic isotope effects of nitrate reduction by periplasmic dissimilatory nitrate reductase

Yuyang He [a,*], Yining Zhang [b], Siting Zhang [c,d], Yun Liu [b,d,e]

[a] *Institute of Mechanics, Chinese Academy of Sciences, Beijing 100190, China*
[b] *State Key Laboratory of Ore Deposit Geochemistry, Institute of Geochemistry, Chinese Academy of Sciences, Guiyang 550081, China*
[c] *Center for Lunar and Planetary Science, Institute of Geochemistry, Chinese Academy of Sciences, Guiyang 550081, China*
[d] *Chinese Academy of Sciences Center for Excellence in Comparative Planetology, Hefei 230001, China*
[e] *International Center for Planetary Science, College of Earth Sciences, Chengdu University of Technology, Chengdu 610059, China*

Received 30 June 2020; accepted in revised form 26 October 2020; available online 4 November 2020

**Abstract**

Kinetic isotope effect (KIE) reveals the transition state structure of an elementary reaction and can be predicted by quantum chemical calculation. Density Functional Theory calculation of an enzymatic reaction with large numbers of atoms is computationally prohibitive, especially if explicit solvent effect is considered. Cutoff method, which simplifies an entire molecule to a cluster around a target position, can simplify position-specific equilibrium isotope effect calculation for a large organic molecule. It should also be applicable to KIE calculation of an enzymatic reaction and allow us to introduce explicit solvent molecules to the system. If this treatment is feasible and trustable, it will provide an efficient method to estimate a number of KIEs produced by enzyme reactions. Obviously, its robustness must be tested. Here, using $NO_3^-$ reduction by the active site of periplasmic dissimilatory nitrate reductase (Nap) in *Rhodobacter sphaeroides* as an example, we built 17 models to test the influence of cutoff size, implicit, and explicit solvent effects on KIE calculation. The results show that to estimate the KIE value of an enzymatic reaction accurately and efficiently, we can first simplify the reaction model to a cutoff model with 3 proximal bonds to the active position. Then, incorporating implicit-plus-explicit solvent models can simulate a reaction environment more realistically, which is necessary for accuracy. Our calculated ln*KIE* values for nitrate Nap reduction at 25 °C are $-32.4 \pm 1.8$‰ for $^{15}N$ and $-20.9 \pm 0.4$ ‰ for $^{18}O$, respectively, with a $\ln^{18}KIE/\ln^{15}KIE$ ratio of $0.65 \pm 0.05$. Although additional reservoir-transport processes need to be considered, our calculation results are consistent with calibrated isotope effects from laboratory experiments, suggesting that the transition state we calculated depicts the general reaction mechanism of $NO_3^-$ reduction by Nap.


*Keywords:* Transition state theory; Density functional theory; Cutoff model; Solvent effect; Molybdenum enzyme

## 1. INTRODUCTION

Global cycling of essential life elements, such as C, N, O, and S, on Earth surface is largely controlled by microorganisms. Understanding enzymatic reaction mechanisms is the fundamental step towards a quantitative assessment of biochemical processes in laboratory experiments, at field observation, as well as during biogeochemical cycling at the global scale.

The key to elucidating the reaction mechanism of an enzymatic reaction is to elaborate its transition state structure. A transition state refers to the saddle point of the potential energy surface for an elemental reaction, where the reaction can take place over the path corresponding to the lowest energy barrier (Eyring, 1935a,b). The molecular structure of such a rate-limiting but unstable transition

* Corresponding author.
*E-mail address:* yhe@imech.ac.cn (Y. He).

https://doi.org/10.1016/j.gca.2020.10.027
0016-7037/

state is the key to understand the integral behavior of biological functions (Wong et al., 2015). However, the elementary steps of an enzymatic reaction are usually unidirectional and occur in nano- and femto- seconds. It is difficult to virtually identify each elementary step of enzymatic processes even in our state-of-the-art laboratories (Williams and Wilson, 2016).

The force field of a compound is independent of its isotope substitutions. Therefore, an isotope fractionation factor between the transition state and reactant, i.e. kinetic isotope effect (KIE), can be used as a unique test of a transition state molecular structure (Bigeleisen and Wolfsberg, 1958; Bigeleisen, 1949). KIE is an intrinsic parameter for an elementary reaction. To be consistent with the definition of equilibrium isotope effect (EIE $= {}^{h}K/{}^{l}K$, where $K$ denotes the equilibrium constants of heavy ($h$) or light ($l$) isotopes), here we use the definition of KIE $= {}^{h}k/{}^{l}k$, where $k$ denotes the reaction rate constants (Jones and Urbauer, 1991; Bao et al., 2016; He et al., 2020b). This definition is opposite to what Bigeleisen (1949) originally defined, and that of commonly used in environmental isotope geochemistry community. Using such definition, a KIE value smaller than 1 or a negative ln$KIE$ value will be called a normal KIE, where light isotopes react faster than heavy isotopes.

Obtaining the vibrational frequencies is the key point for understanding the molecular structure of a transition state complex. Density Functional Theory (DFT) calculation coupled with Urey-Bigeleisen-Mayer model is a reliable approach to identify the transition state for a specific reaction and to estimate its KIE theoretically (Bigeleisen and Mayer, 1947; Urey, 1947; Bigeleisen and Wolfsberg, 1958; Felipe et al., 2001; Liu and Tossell, 2005; Guo et al., 2009; Zeebe, 2014; Zhang and Liu, 2014; Zhang et al., 2020). The calculation results can be used to test the validity of experimental results and guide interpretations of observed isotope fractionation factors. Calculation results can also provide candidates that can be tested by controlled laboratory experiments. In addition, one calculation result of an enzymatic reaction can be used to guide and justify future researches of other similar reactions, since multiple enzymes share similar active site molecular structures. For instance, dimethylsulfoxide reductase (DMSOR) family of molybdenum (Mo) enzyme is found responsible for enzymatic reactions such as reductions of nitrate, chlorate, perchlorate, iodate, and polysulfide, oxidation of arsenite, arsenate, and pyridoxal, dehydrogenation of formate, formylmethanofuran, and xanthine, etc. (Hille, 1996, 2002; Youngblut et al., 2016; Glasser et al., 2018; Crawford et al., 2019; Lv et al., 2020; Yamazaki et al., 2020). If we know the transition state structure of nitrate reduction by nitrate reductase of DMSOR family, such a model can be easily transferred to the KIE calculations of reductions of chlorate, perchlorate, iodate, and polysulfide.

Calculating the KIE of a reaction by quantum chemical methods has a long-existing problem that an enzyme usually contains a large number of atoms, which is computationally prohibitive. Therefore, simplification of enzymatic reaction calculation is the key to broader application of KIE estimation. The first KIE calculation for an enzymatic reaction is the methyl transfer between the sulfur of *S*-adenosylmethionine and oxygen of catecholate (Rodgers et al., 1982). Such calculation used two simplifications: (1) Since it was impossible during that time to include all atoms in proteins in quantum chemical calculation, the system was simplified by cutoff method (Wolfsberg and Stern, 1964; Stern and Wolfsberg, 1966) to a cluster of 17 atoms; and (2) It used bond-energy bond-order vibrational analysis (BEBOVIB) approach (Sims et al., 1977), which simplifies involved diagonalization of the mass-weighted Hessian matrix in Cartesian coordinates (Gwinn, 1971) with empirical relationships between bond order, bond length, and force constants (Johnston, 1966; Burton et al., 1977). Based on the optimized cutoff model cartesian coordinates and force constants calculated by quantum chemistry software, ISOEFF98 (Anisimov and Paneth, 1999) and QUIVER (Saunders et al., 1989) were developed to calculate KIEs of enzymatic reactions.

The cutoff method was widely used to simplify KIE calculations for enzymatic reactions. Assuming the atoms, which are not directly involved in the bond-breaking and bond-formation of a reaction, have only secondary isotope effect, i.e. KIE $\approx$ 1.000 (Bigeleisen and Wolfsberg, 1958), previous works commonly used the cutoff method to reduce the whole system to a cluster around the active position. For instance, DFT calculation of human methionine *S*-adenosyltransferase catalyzed *S*-adenosylmethionine formation from ATP and methionine was simplified to a cutoff model with 26 atoms to estimate its KIE value (Firestone and Schramm, 2017).

While these two programs were successfully applied to enzymatic reaction researches (e.g. Acevedo and Evanseck, 2003; Adamczyk et al., 2011; Firestone and Schramm, 2017; Klajman et al., 2017; Wiest et al., 1994), debates between high calculation precision and affordable computational resources never ceased. Previous research of *cis*-dihydroxylation of nitroaromatic compounds catalyzed by nitrobenzene dioxygenase showed that the activation Gibbs free energies for the same process fluctuated with cutoff sizes, as well as with or without implicit or explicit solvent models (water molecule or protein pieces, Pabis et al., 2014). The sensitivity of calculated KIE values to cutoff sizes leads to the question if a cutoff model with a small number of atoms is adequate to describe the reaction environment (Wolfsberg and Stern, 1964; Stern and Wolfsberg, 1966; Williams, 2012). Some researchers optimized cutoff models with a relatively large number of atoms by lower theoretical levels, then did single-point energy calculation by higher theoretical levels (Wiest et al., 1994; Liao and Siegbahn, 2015; Wei et al., 2017). Such a method can reduce calculation resources, but single-point calculation by a higher theoretical level may produce small imaginary frequencies if the configuration is optimized by a lower theoretical level (Liao and Siegbahn, 2015). Furthermore, a cutoff model simulates an enzymatic reaction in the gaseous phase, which rarely occurs in the biosystem. The interactions between solute and solvent molecules, i.e. short-range solvent effect, and the electrostatic effects caused by polarized solvent molecules, i.e. long-range solvent effect, will affect transition state structure. Therefore, a KIE calculation requires to consider solvent effects. Solvent effects can be simulated implicitly or explicitly. Due to the

limitations in computational capability, KIE calculations of enzymatic reactions usually involve only polarizable continuum models (PCM), which implicitly incorporate solvent effects by electrostatic equations (Wujec and Paneth, 2007; Adamczyk et al., 2011, 2014; Geronimo and Paneth, 2014; Pabis et al., 2014; Liao and Siegbahn, 2015; Rivard et al., 2015; Firestone and Schramm, 2017; Klajman et al., 2017; Wei et al., 2017). Surrounding a target molecule with water molecules and/or protein pieces can simulate a solution environment realistically and would have substantial influences on local configurations and therefore the predicted KIE values (Rustad et al., 2008, 2010; Zhang and Liu, 2014; He and Liu, 2015; Gao et al., 2018). However, the explicit solvent effect has rarely been considered. In this study, we believe that the introduction of solvent molecules into simulations of enzymatic reactions can be achieved with the cutoff method.

Like all laboratory experiments, computational experiments also require careful evaluations and standard protocols. The influences of cutoff size and solvent effects on transition state search, i.e. KIE calculation, need to be rigorously tested. Our previous study showed that the vibrational frequencies of an atom in a large organic molecule in gaseous phase are mostly affected by its proximal surroundings. Thus, the position-specific reduced partition function ratios (RPFR or β factor), which refers to the equilibrium isotope fractionation factor between an atom in a specific bond environment and its atomic form, of the target atom can be properly addressed by the cutoff model with proximal three bonds or one ring (He et al., 2020a). Therefore, the KIE calculation of an enzymatic reaction should be able to be simplified to a cluster, where the active site is located at the center of the cluster with close proximal surroundings.

For quantum chemical calculations, the theoretical level and basis set can directly affect the results of geometry optimization, single-point energy, and vibrational frequencies. However, the calculation of large molecular size with high theoretical levels is even more restricted by current computational resources. The efficiency and accuracy of calculating equilibrium isotope effect (EIE) of large organic molecules by DFT has been rigorously tested before (Iron and Gropp, 2019). KIE is the relative isotope enrichment between the transition state and reactant. Compare to an absolute β value, the KIE value should cancel more calculation errors, such as scaling factors for vibrational frequency. Therefore, theoretically, the KIE value is expected to be less sensitive to theoretical level, and a relatively smaller basis set can still accurately predict a KIE value. Examination of theoretical levels confirmed that B3LYP hybrid exchange-correlation functional is robust for enzymatic reaction KIE calculation (Adamczyk et al., 2011; Klajman et al., 2017). In addition, previous works also showed that estimated KIE values are not sensitive to basis sets (Wiest et al., 1994; Adamczyk et al., 2011). Thus, we do not test the influences of theoretical level and basis set in this work.

Nitrate is a key component in global nitrogen cycle and an important source of biologically available nitrogen. Quantitative assessment of nitrate reduction, which is the initial step of nitrogen fixation, provides significant information on understanding global nitrogen cycle. Periplasmic dissimilatory nitrate reductase (Nap) is a Mo containing enzyme that belongs to the DMSOR family. Its structure coordinates have been determined (Dias et al., 1999; Hille, 2002; Jormakka et al., 2004), which can be directly used for KIE calculation. The nitrogen (N) and oxygen (O) KIE values of $NO_3^-$ reduction by Nap have been calibrated by laboratory experiments (Granger et al., 2008; Karsh et al., 2012; Carlisle et al., 2014; Frey et al., 2014; Treibergs and Granger, 2017), which can be used to test calculation results. Therefore, here, we use $NO_3^-$ reduction to $NO_2^-$ by the active site of Nap as an example to test the influence of cutoff size and solvent effects on the KIE calculation of enzymatic reaction by the quantum chemical calculation method.

## 2. METHODS

### 2.1. Nitrate reduction by Nap

Nap is a mononuclear Mo enzyme. Its active site has two tricyclic pyranpterin cofactors (L) bound to the Mo atom, which is the attribute of DMSOR family. The Mo coordination sphere is completed by a cysteine (Cys) and a single Mo═O group in an $L_2Mo^{VI}S$ core (Fig. 1, Hille, 1996, 2002; Dias et al., 1999; Jormakka et al., 2004; Sparacino-Watkins et al., 2014; Cerqueira et al., 2015).

The proposed mechanism of nitrate reduction by Nap involves a series of electron, oxygen, and hydrogen transfer processes (Richardson et al., 2001; Cerqueira et al., 2009, 2015; Biaso et al., 2012; Weinberg et al., 2012; Sparacino-Watkins et al., 2014; Coelho and Romão, 2015). The Nap shall first have two hydrogens and two electrons from external reductant species to the metal site. This leads to the dissociation of the Mo═O oxygen (at the moment of dissociation, as a water molecule). After oxygen dissociation, the enzyme is at a chemically active state with −1 valence (Fig. 2A). Nitrate that promptly occupies a free position near Mo will bind with the active site and form a $(NO_2)$─O─Mo(VI) complex (Fig. 2B). In the next step, the N─O bond will break and release nitrite (Fig. 2C).

The nitrogen and oxygen isotope fractionations of $NO_3^-$ during this process are caused by two steps: (1) free $NO_3^-$ in solution binds with the activated Nap, and (2) $NO_3^-$ on Nap reduces to $NO_2^-$. Such an enzyme-substrate reaction can be described by the pre-equilibrium approximation: an enzyme $E$ binds with a substrate $S$ to produce an enzyme-substrate complex intermediate $ES$, which then forms a product $P$. The $ES$ complex consumption rate constant ($k_2$) is relatively small compared to the forward and backward reaction rate constants between $E+S$ and $ES$ ($k_1$ and $k_{-1}$), and the backward reaction of $ES$ complex consumption is negligible ($k_{-2} \ll k_2$) (Galimov, 2006; Turányi and Tomlin, 2014). Such a process can thus be expressed as

$$E + S \underset{k_{-1}}{\overset{k_1}{\rightleftarrows}} ES \xrightarrow{k_2} E + P \quad (1)$$

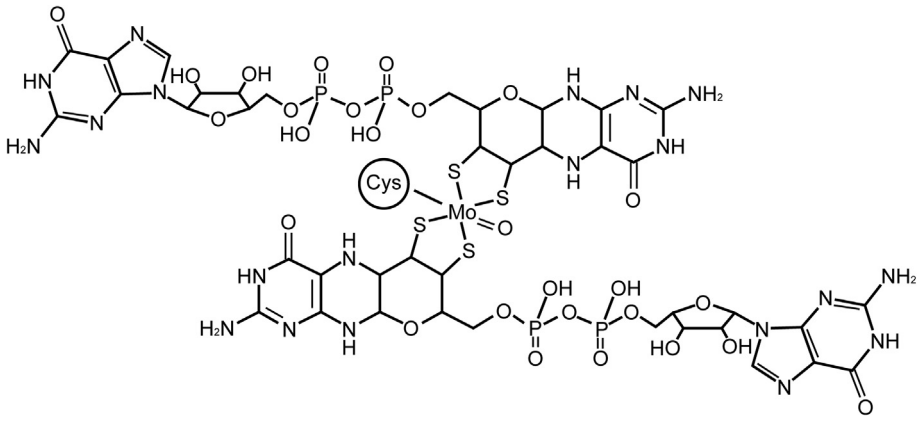


Fig. 1. Active site molecular structure of Nap nitrate reductase, Cys = Cysteine (Modified from Arnoux et al., 2003; Sparacino-Watkins et al., 2014; Tejada-Jimenez et al., 2018).

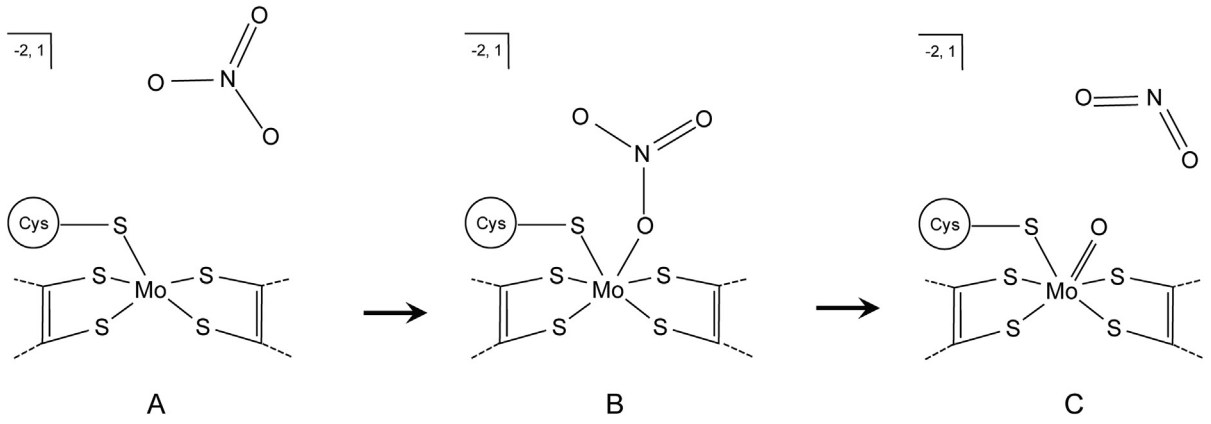


Fig. 2. Proposed nitrate reduction mechanism by Nap nitrate reductase. –2 is the total valance and 1 is the spin multiplicity of the system (Modified from Biaso et al., 2012; Coelho and Romão, 2015; Cerqueira et al., 2009, 2015; Jepson et al., 2007; Niks and Hille, 2019; Richardson et al., 2001; Sparacino-Watkins et al., 2014; Weinberg et al., 2012).

Using the pre-equilibrium approximation, the *ES* can be assumed to be in equilibrium with $E + S$, and the production of $P$ can be considered uni-directional. In our case, after the equilibration between $NO_3^-$-enzyme complex and $NO_3^-$ in solution, $NO_2^-$ is produced uni-directionally. The apparent isotope fractionation of nitrate reduction by Nap ($\alpha_{Nap}$) equals to the sum of the EIE of $NO_3^-$-enzyme with $NO_3^-$ in solution and the KIE of the N—O bond-breaking process. This study focuses on the validation of the KIE calculation method for enzymatic reactions. Thus, we do not provide calculation details of aqueous phase $NO_3^-$ here.

## 2.2. Calculation details

### 2.2.1. Calculation models

The enzyme structure used in this study has been adopted and modified from the active center coordinates of *Rhodobacter sphaeroides* NapA enzyme (PDB ID: 1OGY, Arnoux et al., 2003). To test the influence of cutoff size, implicit, and explicit solvent effects on KIE calculation, 17 models have been built and calculated independently (Table 1).

Three enzyme clusters with 65 ($NapA_L$), 45 ($NapA_M$), and 29 ($NapA_S$) atoms (Fig. 3, top panel) are built based on the optimized structure of 1OGY active center (see SI for the structure coordinates of the optimized active center at chemically activated state with −1 valence). All bonds that have been cut are single bonds and have been balanced by a hydrogen atom. Two self-consistent reaction field approach: integral-equation-formalism polarizable continuum model (IEFPCM) (Scalmani and Frisch, 2010) and solvation model density (SMD) (Marenich et al., 2009), have been used on the $NapA_S$ model to evaluate the implicit solvent effect by comparing the results with the ideal gas state calculation results. To test the errors arisen from the explicit solvent effect, we have also performed calculations for the $NapA_S$ model by adding additional 3, 6, 9, 12 explicit water molecules (Fig. 3, bottom panel).

### 2.2.2. Ab initio calculation

All geometry optimization and harmonic vibrational frequencies calculation for ground states have been performed in software Gaussian16 (Frisch et al., 2016). In this study, all calculations have been carried out at the DFT level using

Table 1
Descriptions of calculation models.

| Model | Atom number | Explicit water | Implicit solvent effect |
|---|---|---|---|
| $NapA_L$ | 65 | 0 | NA |
| $NapA_M$ | 45 | 0 | NA |
| $NapA_S$ | 29 | 0 | NA/SMD/IEFPCM |
| $NapA_S(H_2O)_3$ | 38 | 3 | NA/SMD/IEFPCM |
| $NapA_S(H_2O)_6$ | 47 | 6 | NA/SMD/IEFPCM |
| $NapA_S(H_2O)_9$ | 56 | 9 | NA/SMD/IEFPCM |
| $NapA_S(H_2O)_{12}$ | 65 | 12 | NA/SMD/IEFPCM |

Note: L denotes cluster models with 65 atoms; M denotes cluster models with 45 atoms; and S denotes cluster models with 29 atoms.

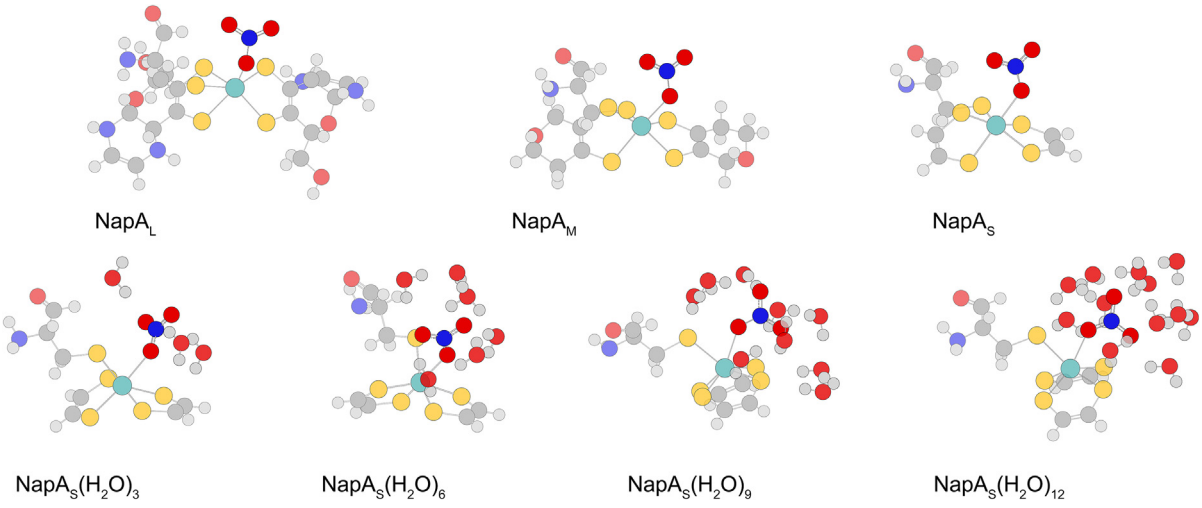


Fig. 3. Representative $NO_3^-$-NapA models with cutoff sizes of 65 ($NapA_L$), 45 ($NapA_M$), and 29 ($NapA_S$) atoms (top panel), and $NO_3^-$-NapAs models with 3 ($NapA_S(H_2O)_3$), 6 ($NapA_S(H_2O)_6$), 9 ($NapA_S(H_2O)_9$), and 12 ($NapA_S(H_2O)_{12}$) explicit water molecules. Dark gray, light gray, red, yellow, blue, and green spheres represent C, H, O, S, N, and Mo atoms, respectively. (For interpretation of the references to colour in this figure legend, the reader is referred to the web version of this article.)

B3LYP hybrid exchange-correlation functional (Lee et al., 1988; Becke, 1993). 6-31+g(d,p) basis set (Frisch et al., 1984), which is widely used in the DFT studies of enzymatic reactions (e.g. Wujec and Paneth, 2007; Adamczyk et al., 2011, 2014; Klajman et al., 2017), has been used for C, H, O, N, and S atoms. LANL2DZ-ECP basis set with effective core potential (Hay and Wadt, 1985; Wadt and Hay, 1985) has been used for the Mo atom in enzymes to save some computational efforts with negligible loss of accuracy. Scaling factors are not considered since they are largely canceled in the reported KIE values (Schauble et al., 2006; Méheut et al., 2007). The reactant ($NO_3$-NapA complex) structures are optimized to local minimum without imaginary frequency except for the $NO_3^-$-$NapA_S(H_2O)_6$ model with SMD implicit solvent effect, which has a small imaginary frequency of $6.6i$ $cm^{-1}$. This small imaginary frequency does not significantly affect the zero-point energy and thus has been disregarded. Based on the optimized reactant structures, we build initial guess structures (TS-NapA complex) for transition states search with Berny algorithm (Schlegel, 1982), i.e. TS method in Gaussian16. All transition state structures are optimized to a saddle point with exactly one imaginary frequency along the O—N decomposition path.

*2.2.3. KIE calculation*

Based on the optimized structures, we calculated $\beta$ values for reactant ($\beta_{NO_3^- - NapA}$) and transition state ($\beta_{TS-NapA}$) at 25 °C for the nitrogen and three oxygen atoms of $NO_3^-$.

$\beta_{NO_3^- - NapA}$ have been calculated with harmonic approximation using Urey- Bigeleisen-Mayer model (Bigeleisen and Mayer, 1947; Urey, 1947):

$$\beta_{NO_3^- - NapA} = \prod_i^{3n-6} \left(\frac{u_i^*}{u_i}\right)\left(\frac{e^{-u_i^*/2}}{e^{-u_i/2}}\right)\left(\frac{1-e^{-u_i}}{1-e^{-u_i^*}}\right) \quad (2)$$

$$u_i = \frac{h\upsilon_i}{k_B T} \quad (3)$$

where the superscript "*" indicates rare isotope ($^{15}N$ and $^{18}O$) substituted molecules and the one without superscript is the reference isotope ($^{14}N$ and $^{16}O$), $\upsilon_i$ denotes the $i^{th}$ harmonic vibration frequency, $h$ denotes the Planck constant, $k_B$ denotes the Boltzmann constant, and $T$ denotes the temperature in K, and $n$ is the total number of atoms.

$\beta_{TS-NapA}$ have been calculated using Bigeleisen model (Bigeleisen, 1949; Bigeleisen and Wolfsberg, 1958):

$$\beta_{TS-NapA} = \frac{\upsilon_L^*}{\upsilon_L} \prod_i^{3n-7} \left(\frac{u_i^*}{u_i}\right)\left(\frac{e^{-u_i^*/2}}{e^{-u_i/2}}\right)\left(\frac{1-e^{-u_i}}{1-e^{-u_i^*}}\right) \quad (4)$$

where $v_L$ denotes the imaginary frequency along the path of decomposition.

The average values for the three oxygens are also reported since the observed isotope fractionations are compound-specific. The $\beta$ value differences are discussed in terms of $\ln(\beta_A/\beta_B)$ in per mil, where A and B denote the two models in comparison.

KIE have been calculated by Eq. (5):

$$KIE = \frac{\beta_{TS-NapA}}{\beta_{NO_3^- -NapA}} \quad (5)$$

For better illustration, we report KIE values as $\ln KIE$ in per mil. The KIE value difference is also reported as $\ln(KIE_A/KIE_B)$ in per mil. In addition to single KIE values, the relationships between the KIEs of nitrogen and oxygens in $NO_3^-$, i.e. $^{18}\ln KIE$: $^{15}\ln KIE$ values, are also reported.

## 3. RESULTS

### 3.1. Optimized Structures for reactants and transition states

The optimized active position structures (Mo—$ONO_2$ complex) with selected geometric parameters for reactant and transition states are shown in Tables 2, 3, and Fig. 4. Among the three oxygens, $O_a$ denotes the oxygen binds with Mo atom, which is the O2 atom in structure coordinates. $O_b$ and $O_c$ denote O3 and O4 atoms in structure coordinates, respectively (See SI for the optimized structure coordinates).

The active position structures of the reactant complex vary in a small range (Table 2, Fig. 4A). Among all models, the standard deviations of N—O bond lengths and ∠O—N—O angles are smaller than 0.01 Å and 0.8°, respectively. The largest uncertainty is the Mo—$O_a$ bond length, d (Mo—$O_a$), and the ∠Mo—$O_a$—N angle in the reactant structure, which are $2.35 \pm 0.10$ Å and $133.1 \pm 3.0$°, respectively. Implicit solvation effects introduce ~0.2 Å variations on d(Mo—$O_a$) when a model has 3 or 6 explicit water molecules. Such influence disappears when a model has 9 or 12 explicit water molecules (0.01 Å). Both implicit and explicit solvent effects cause variations on ∠Mo—$O_a$—N. This is largely due to the electrostatic effects and hydrogen bonds among the $NO_3^-$ and explicit solvent molecules.

Nitrate reduction is the dissociation of the $O_a$—N bond. Our calculation results predict an elongation of the $O_a$—N bond from $1.28 \pm 0.01$ Å of the reactant to $1.75 \pm 0.02$ Å of the transition state, accompanied by the shortening of the Mo—$O_a$ bond from $2.35 \pm 0.10$ Å of the reactant to $1.90 \pm 0.02$ Å of the transition state. Similar to reactant structures, explicit solvent molecules also cause relatively large uncertainty on the ∠Mo—$O_a$—N angle of transition state structures (128.2°) with a standard deviation of 2.9°.

### 3.2. $\beta_{NO_3^- -NapA}$ factors

The calculated $\beta_{NO_3^- -NapA}$ values at 25 °C are 1.1540 ± 0.0031 for $^{15}$N, and 1.0986 ± 0.0014 for $^{18}O_{ave}$ (Table 4). Without solvent effects, cutoff size has limited effects on the calculated $\beta_{NO_3^- -NapA}$ value, where $\ln(\beta_{NO_3^- -NapA_M}/\beta_{NO_3^- -NapA_L})$ are 0.8‰ for $^{15}$N and −0.7‰ for $^{18}O_{ave}$, and $\ln(\beta_{NO_3^- -NapA_S}/\beta_{NO_3^- -NapA_M})$ are 0.0‰ for $^{15}$N and 0.0‰ for $^{18}O_{ave}$. Such variations are both significantly smaller than the standard deviation of different $\beta_{NO_3^- -NapA}$ values.

Compare to the cutoff sizes, implicit solvent effects have relatively larger influences on the calculated $\beta_{NO_3^- -NapA}$ values. For models with the same number of explicit water molecules, SMD implicit solvent effect introduces maxi-

Table 2
Selected geometric parameters (d – distances in Å, ∠– angles in °) of $NO_3^-$-NapA complexes.

| Model | Implicit solvent effect | d(Mo—$O_a$) | d($O_a$—N) | d(N—$O_b$) | d(N—$O_c$) | ∠Mo—$O_a$—N | ∠$O_a$—N—$O_b$ | ∠$O_a$—N—$O_c$ | ∠$O_b$—N—$O_c$ |
|---|---|---|---|---|---|---|---|---|---|
| $NO_3^-$-$NapA_L$ | NA | 2.21 | 1.31 | 1.25 | 1.24 | 131.8 | 116.2 | 120.6 | 123.2 |
| $NO_3^-$-$NapA_M$ | NA | 2.28 | 1.30 | 1.25 | 1.24 | 127.7 | 117.2 | 120.3 | 122.4 |
| $NO_3^-$-$NapA_S$ | NA | 2.28 | 1.29 | 1.25 | 1.25 | 128.6 | 117.4 | 120.4 | 122.2 |
| $NO_3^-$-$NapA_S$ | SMD | 2.53 | 1.27 | 1.26 | 1.25 | 130.3 | 118.6 | 120.9 | 120.5 |
| $NO_3^-$-$NapA_S$ | IEFPCM | 2.35 | 1.29 | 1.26 | 1.25 | 128.8 | 117.6 | 120.6 | 121.7 |
| $NO_3^-$-$NapA_S(H_2O)_3$ | NA | 2.37 | 1.28 | 1.25 | 1.26 | 133.0 | 118.2 | 120.8 | 121.1 |
| $NO_3^-$-$NapA_S(H_2O)_3$ | SMD | 2.53 | 1.26 | 1.27 | 1.25 | 131.4 | 118.1 | 121.6 | 120.2 |
| $NO_3^-$-$NapA_S(H_2O)_3$ | IEFPCM | 2.42 | 1.27 | 1.26 | 1.26 | 131.9 | 118.5 | 120.7 | 120.7 |
| $NO_3^-$-$NapA_S(H_2O)_6$ | NA | 2.38 | 1.27 | 1.27 | 1.25 | 135.5 | 117.1 | 121.8 | 121.0 |
| $NO_3^-$-$NapA_S(H_2O)_6$ | SMD | 2.52 | 1.26 | 1.27 | 1.25 | 133.3 | 118.2 | 121.6 | 120.2 |
| $NO_3^-$-$NapA_S(H_2O)_6$ | IEFPCM | 2.44 | 1.26 | 1.27 | 1.25 | 137.6 | 117.5 | 121.8 | 120.7 |
| $NO_3^-$-$NapA_S(H_2O)_9$ | NA | 2.28 | 1.28 | 1.26 | 1.25 | 136.8 | 116.9 | 121.3 | 121.8 |
| $NO_3^-$-$NapA_S(H_2O)_9$ | SMD | 2.28 | 1.28 | 1.26 | 1.24 | 135.2 | 116.4 | 121.8 | 121.8 |
| $NO_3^-$-$NapA_S(H_2O)_9$ | IEFPCM | 2.27 | 1.28 | 1.26 | 1.24 | 135.1 | 116.7 | 121.5 | 121.8 |
| $NO_3^-$-$NapA_S(H_2O)_{12}$ | NA | 2.28 | 1.28 | 1.27 | 1.24 | 136.5 | 116.7 | 121.8 | 121.5 |
| $NO_3^-$-$NapA_S(H_2O)_{12}$ | SMD | 2.29 | 1.28 | 1.26 | 1.24 | 134.7 | 116.9 | 121.6 | 121.5 |
| $NO_3^-$-$NapA_S(H_2O)_{12}$ | IEFPCM | 2.29 | 1.28 | 1.27 | 1.24 | 134.3 | 116.8 | 121.6 | 121.6 |
| Average* | | 2.35 | 1.28 | 1.26 | 1.25 | 133.1 | 117.4 | 121.2 | 121.4 |
| Stdv. | | 0.10 | 0.01 | 0.01 | 0.01 | 3.0 | 0.7 | 0.6 | 0.8 |

* The "Average" data are the mean values of all models, and the "Stdv" data are the standard deviation of all models.

Table 3
Selected geometric parameters (d – distances in Å, ∠ – angles in °) of TS-NapA complexes.

| Model | Implicit solvent effect | d(Mo—$O_a$) | d($O_a$-N) | d(N—$O_b$) | d(N—$O_c$) | ∠Mo—$O_a$—N | ∠$O_b$—N—$O_c$ |
|---|---|---|---|---|---|---|---|
| TS -$NapA_L$ | NA | 1.87 | 1.77 | 1.22 | 1.21 | 126.4 | 127.1 |
| TS -$NapA_M$ | NA | 1.87 | 1.80 | 1.22 | 1.22 | 128.2 | 126.4 |
| TS-$NapA_S$ | NA | 1.89 | 1.74 | 1.22 | 1.21 | 126.7 | 126.7 |
| TS-$NapA_S$ | SMD | 1.92 | 1.73 | 1.23 | 1.21 | 126.0 | 126.1 |
| TS-$NapA_S$ | IEFPCM | 1.89 | 1.76 | 1.22 | 1.22 | 126.8 | 126.7 |
| TS-$NapA_S(H_2O)_3$ | NA | 1.90 | 1.73 | 1.22 | 1.23 | 134.7 | 124.7 |
| TS-$NapA_S(H_2O)_3$ | SMD | 1.92 | 1.73 | 1.24 | 1.22 | 129.4 | 124.0 |
| TS-$NapA_S(H_2O)_3$ | IEFPCM | 1.90 | 1.75 | 1.23 | 1.22 | 128.3 | 124.5 |
| TS-$NapA_S(H_2O)_6$ | NA | 1.90 | 1.72 | 1.23 | 1.22 | 135.0 | 124.3 |
| TS-$NapA_S(H_2O)_6$ | SMD | 1.92 | 1.72 | 1.24 | 1.23 | 128.5 | 123.5 |
| TS-$NapA_S(H_2O)_6$ | IEFPCM | 1.90 | 1.73 | 1.24 | 1.23 | 129.9 | 123.6 |
| TS-$NapA_S(H_2O)_9$ | NA | 1.90 | 1.74 | 1.22 | 1.22 | 128.0 | 126.0 |
| TS-$NapA_S(H_2O)_9$ | SMD | 1.89 | 1.76 | 1.23 | 1.21 | 127.5 | 126.3 |
| TS-$NapA_S(H_2O)_9$ | IEFPCM | 1.88 | 1.78 | 1.22 | 1.21 | 128.0 | 126.2 |
| TS-$NapA_S(H_2O)_{12}$ | NA | 1.90 | 1.75 | 1.24 | 1.21 | 124.9 | 125.7 |
| TS-$NapA_S(H_2O)_{12}$ | SMD | 1.91 | 1.76 | 1.23 | 1.21 | 125.6 | 125.9 |
| TS-$NapA_S(H_2O)_{12}$ | IEFPCM | 1.91 | 1.76 | 1.23 | 1.21 | 125.6 | 126.0 |
| Average* | | 1.90 | 1.75 | 1.23 | 1.22 | 128.2 | 125.5 |
| Stdv | | 0.02 | 0.02 | 0.01 | 0.01 | 2.9 | 1.2 |

* The "Average" data are the mean values of all models, and the "Stdv" data are the standard deviation of all models.

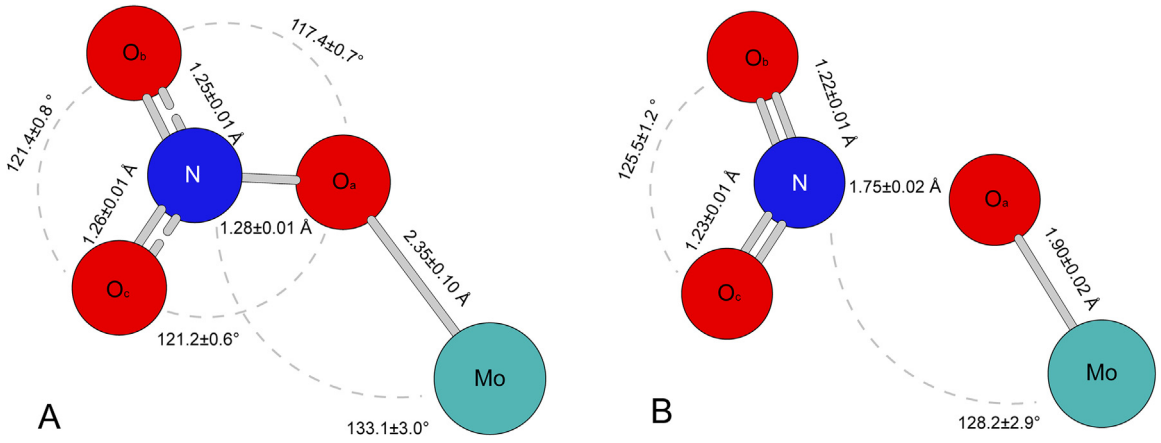


Fig. 4. Optimized active position structures (Mo—$ONO_2$ complex) with selected geometric parameters for reactant (A) or transition state (B). Geometric parameters are the average of 17 models with different cutoff sizes, implicit, and/or explicit solvent effects.

mum $\beta_{NO_3^- - NapA}$ value variations of 6.9‰ on $^{15}N$ and 2.5‰ on $^{18}O_{ave}$, and IEFPCM implicit solvent effect introduces maximum $\beta_{NO_3^- - NapA}$ value variations of 3.5‰ on $^{15}N$ and 1.6‰ on $^{18}O_{ave}$.

For models with or without the same implicit solvent effect, adding explicit water molecules introduce maximum $\beta_{NO_3^- - NapA}$ value variations of 3.5‰ on both $^{15}N$ and $^{18}O_{ave}$. However, there are limited $\beta_{NO_3^- - NapA}$ value variations among models with different explicit water molecule number. The four explicit solvent models without implicit solvent effect have maximum differences of 0.7‰ for $^{15}N$ and 1.5‰ for $^{18}O_{ave}$. The four explicit solvent models with SMD implicit solvent effect have maximum differences of 1.3‰ for $^{15}N$ and 1.7‰ for $^{18}O_{ave}$. The four explicit solvent models with IEFPCM implicit solvent effect have maximum differences of 1.6‰ for $^{15}N$ and 2.5‰ for $^{18}O_{ave}$.

### 3.3. $\beta_{TS-NapA}$ factors

The calculated $\beta_{TS-NapA}$ values at 25 °C are 1.1190 ± 0.0036 for $^{15}N$, and 1.0769 ± 0.0014 for $^{18}O_{ave}$ (Table 5). Without solvent effects, cutoff size also has limited effects on the calculated $\beta_{TS-NapA}$ value, where $\ln(\beta_{TS-NapA_M}/\beta_{TS-NapA_L})$ are −1.8‰ for $^{15}N$ and −0.9‰ for $^{18}O_{ave}$, and $\ln(\beta_{TS-NapA_S}/\beta_{TS-NapA_M})$ are 1.3‰ for $^{15}N$ and 0.6‰ for $^{18}O_{ave}$.

Implicit solvent effects have similar influences on the calculated $\beta_{TS-NapA}$ values as on the calculated $\beta_{NO_3^- - NapA}$ values. For the same explicit solvent models, SMD implicit solvent effect introduces a maximum $\beta_{TS-NapA}$ value variation of 8.9‰ on $^{15}N$ and 5.1‰ on $^{18}O_{ave}$; IEFPCM implicit solvent effect introduces a maximum $\beta_{TS-NapA}$ value variation of 3.7‰ on $^{15}N$ and 1.9‰ on $^{18}O_{ave}$.

Table 4
Calculated $\beta_{NO_3^- - NapA}$ values at 25 °C.

| Model | Implicit solvent effect | $^{15}N$ | $^{18}O_a$ | $^{18}O_b$ | $^{18}O_c$ | $^{18}O_{ave}$ |
|---|---|---|---|---|---|---|
| $NO_3^-$-$NapA_L$ | NA | 1.1547 | 1.0924 | 1.0996 | 1.1037 | 1.0986 |
| $NO_3^-$-$NapA_M$ | NA | 1.1556 | 1.0951 | 1.0977 | 1.1006 | 1.0978 |
| $NO_3^-$-$NapA_S$ | NA | 1.1556 | 1.0957 | 1.0975 | 1.1001 | 1.0978 |
| $NO_3^-$-$NapA_S$ | SMD | 1.1477 | 1.0975 | 1.0920 | 1.0975 | 1.0957 |
| $NO_3^-$-$NapA_S$ | IEFPCM | 1.1516 | 1.0961 | 1.0958 | 1.0997 | 1.0972 |
| $NO_3^-$-$NapA_S(H_2O)_3$ | NA | 1.1574 | 1.1003 | 1.0970 | 1.1013 | 1.0995 |
| $NO_3^-$-$NapA_S(H_2O)_3$ | SMD | 1.1497 | 1.0996 | 1.0922 | 1.0982 | 1.0967 |
| $NO_3^-$-$NapA_S(H_2O)_3$ | IEFPCM | 1.1543 | 1.1012 | 1.0977 | 1.0978 | 1.0989 |
| $NO_3^-$-$NapA_S(H_2O)_6$ | NA | 1.1578 | 1.1029 | 1.0948 | 1.1010 | 1.0996 |
| $NO_3^-$-$NapA_S(H_2O)_6$ | SMD | 1.1512 | 1.1022 | 1.0930 | 1.0986 | 1.0979 |
| $NO_3^-$-$NapA_S(H_2O)_6$ | IEFPCM | 1.1549 | 1.1020 | 1.0937 | 1.0992 | 1.0983 |
| $NO_3^-$-$NapA_S(H_2O)_9$ | NA | 1.1571 | 1.0997 | 1.0986 | 1.1017 | 1.1000 |
| $NO_3^-$-$NapA_S(H_2O)_9$ | SMD | 1.1505 | 1.0970 | 1.0944 | 1.1025 | 1.0980 |
| $NO_3^-$-$NapA_S(H_2O)_9$ | IEFPCM | 1.1542 | 1.0983 | 1.0969 | 1.1028 | 1.0993 |
| $NO_3^-$-$NapA_S(H_2O)_{12}$ | NA | 1.1579 | 1.1004 | 1.0967 | 1.1061 | 1.1011 |
| $NO_3^-$-$NapA_S(H_2O)_{12}$ | SMD | 1.1510 | 1.0976 | 1.0968 | 1.1014 | 1.0986 |
| $NO_3^-$-$NapA_S(H_2O)_{12}$ | IEFPCM | 1.1561 | 1.1017 | 1.0962 | 1.1051 | 1.1010 |
| Average* | | 1.1540 | 1.0988 | 1.0959 | 1.1010 | 1.0986 |
| Stdv | | 0.0031 | 0.0029 | 0.0022 | 0.0025 | 0.0014 |
| Preferred value** | | 1.1549 ±0.0008 | | | | 1.0994 ±0.0010 |

* The "Average" data are the mean values of all models, and the "Stdv" data are the standard deviation of all models;
** The "preferred value" is the average results of four explicit $NO_3^-$-$NapA_S(H_2O)_n$ models with IEFPCM implicit solvent effect.

Table 5
Calculated $\beta_{TS-NapA}$ values at 25 °C.

| Model | Implicit solvent effect | $^{15}N$ | $^{18}O_a$ | $^{18}O_b$ | $^{18}O_c$ | $^{18}O_{ave}$ |
|---|---|---|---|---|---|---|
| TS-$NapA_L$ | NA | 1.1237 | 1.0422 | 1.0960 | 1.0977 | 1.0786 |
| TS-$NapA_M$ | NA | 1.1217 | 1.0417 | 1.0948 | 1.0963 | 1.0776 |
| TS-$NapA_S$ | NA | 1.1232 | 1.0408 | 1.0955 | 1.0982 | 1.0782 |
| TS-$NapA_S$ | SMD | 1.1161 | 1.0381 | 1.0902 | 1.0954 | 1.0746 |
| TS-$NapA_S$ | IEFPCM | 1.1189 | 1.0398 | 1.0934 | 1.0958 | 1.0763 |
| TS-$NapA_S(H_2O)_3$ | NA | 1.1221 | 1.0408 | 1.0977 | 1.0967 | 1.0784 |
| TS-$NapA_S(H_2O)_3$ | SMD | 1.1122 | 1.0408 | 1.0890 | 1.0934 | 1.0744 |
| TS-$NapA_S(H_2O)_3$ | IEFPCM | 1.1164 | 1.0420 | 1.0918 | 1.0955 | 1.0764 |
| TS-$NapA_S(H_2O)_6$ | NA | 1.1210 | 1.0405 | 1.0951 | 1.0984 | 1.0780 |
| TS-$NapA_S(H_2O)_6$ | SMD | 1.1124 | 1.0419 | 1.0905 | 1.0931 | 1.0752 |
| TS-$NapA_S(H_2O)_6$ | IEFPCM | 1.1154 | 1.0422 | 1.0931 | 1.0942 | 1.0765 |
| TS-$NapA_S(H_2O)_9$ | NA | 1.1213 | 1.0399 | 1.0972 | 1.0958 | 1.0776 |
| TS-$NapA_S(H_2O)_9$ | SMD | 1.1169 | 1.0390 | 1.0909 | 1.0970 | 1.0756 |
| TS-$NapA_S(H_2O)_9$ | IEFPCM | 1.1197 | 1.0405 | 1.0936 | 1.0967 | 1.0769 |
| TS-$NapA_S(H_2O)_{12}$ | NA | 1.1226 | 1.0411 | 1.0933 | 1.1029 | 1.0791 |
| TS-$NapA_S(H_2O)_{12}$ | SMD | 1.1184 | 1.0391 | 1.0909 | 1.0998 | 1.0766 |
| TS-$NapA_S(H_2O)_{12}$ | IEFPCM | 1.1209 | 1.0403 | 1.0926 | 1.1013 | 1.0781 |
| Average* | | 1.1190 | 1.0406 | 1.0933 | 1.0970 | 1.0769 |
| Stdv | | 0.0036 | 0.0012 | 0.0025 | 0.0026 | 0.0014 |
| Preferred value** | | 1.1181 ±0.0023 | | | | 1.0770 ±0.0007 |

* The "Average" data are the mean values of all models, and the "Stdv" data are the standard deviation of all models;
** The "preferred value" is the average results of four explicit $NO_3^-$-$NapA_S(H_2O)_n$ models with IEFPCM implicit solvent effect.

For models with or without the same implicit solvent effect, adding explicit water molecules introduces a maximum $\beta_{TS-NapA}$ value variation of 4.0‰ on both $^{15}N$ and 1.7‰ on $^{18}O_{ave}$. Among the four explicit solvent models without implicit solvent effect, the maximum $\beta_{TS-NapA}$ value variations are 0.7‰ on $^{15}N$ and 1.5‰ on $^{18}O_{ave}$. However, the four explicit solvent models with SMD implicit solvent effect have maximum variations of 4.0‰ on $^{15}N$ and 2.0‰ on $^{18}O_{ave}$, and the four explicit solvent models with IEFPCM implicit solvent effect have maximum differences of 4.9‰ for $^{15}N$ and 1.6‰ for $^{18}O_{ave}$.

### 3.4. Kinetic isotope fractionation of nitrate Nap-reduction

The calculated ln*KIE* values at 25 °C are $-30.8 \pm 2.3$‰ for $^{15}N$, and $-20.2 \pm 0.9$‰ for $^{18}O_{ave}$, with $\ln^{18}KIE$: $\ln^{15}KIE = 0.66 \pm 0.04$ (Table 6, Fig. 5). As expected, only the N and $O_a$ atoms that directly involved in the bond-breaking process have primary isotope effects ($\ln^{18}KIE_{Oa} = -54.4 \pm 2.8$‰), while $O_b$ and $O_c$ only have $-5.5$ – 0.6‰ secondary isotope effects.

Reducing cluster size influence more on the calculated $^{15}$KIE, but it does not affect $^{18}$KIE much. The $\ln(KIE_{NapA_M}/KIE_{NapA_L})$ values are −2.6‰ for $^{15}N$ and −0.2‰ for $^{18}O_{ave}$, and the $\ln(KIE_{NapA_S}/KIE_{NapA_M})$ values are 1.4‰ for $^{15}N$ and 0.5‰ for $^{18}O_{ave}$.

Table 6
Calculated ln*KIE* (‰) values of $NO_3^-$ reduction by NapA at 25 °C.

| Model | Implicit solvent effect | $^{15}N$ | $^{18}O_a$ | $^{18}O_b$ | $^{18}O_c$ | $^{18}O_{ave}$ | $^{18}O_{ave}$: $^{15}N$ |
|---|---|---|---|---|---|---|---|
| $NapA_L$ | NA | −27.2 | −47.0 | −3.3 | −5.5 | −18.6 | 0.68 |
| $NapA_M$ | NA | −29.8 | −50.0 | −2.6 | −3.9 | −18.8 | 0.63 |
| $NapA_S$ | NA | −28.4 | −51.4 | −1.8 | −1.7 | −18.3 | 0.64 |
| $NapA_S$ | SMD | −27.9 | −55.6 | −1.6 | −1.9 | −19.7 | 0.71 |
| $NapA_S$ | IEFPCM | −28.8 | −52.7 | −2.2 | −3.6 | −19.5 | 0.68 |
| $NapA_S(H_2O)_3$ | NA | −31.0 | −55.6 | 0.6 | −4.2 | −19.7 | 0.64 |
| $NapA_S(H_2O)_3$ | SMD | −33.2 | −55.0 | −2.9 | −4.4 | −20.8 | 0.63 |
| $NapA_S(H_2O)_3$ | IEFPCM | −33.4 | −55.3 | −5.4 | −2.1 | −20.9 | 0.63 |
| $NapA_S(H_2O)_6$ | NA | −32.3 | −58.2 | 0.3 | −2.4 | −20.1 | 0.62 |
| $NapA_S(H_2O)_6$ | SMD | −34.3 | −56.3 | −2.3 | −5.0 | −21.2 | 0.62 |
| $NapA_S(H_2O)_6$ | IEFPCM | −34.8 | −55.8 | −0.5 | −4.6 | −20.3 | 0.58 |
| $NapA_S(H_2O)_9$ | NA | −31.4 | −55.9 | −1.3 | −5.4 | −20.9 | 0.67 |
| $NapA_S(H_2O)_9$ | SMD | −29.6 | −54.3 | −3.2 | −5.0 | −20.8 | 0.70 |
| $NapA_S(H_2O)_9$ | IEFPCM | −30.3 | −54.1 | −3.0 | −5.5 | −20.9 | 0.69 |
| $NapA_S(H_2O)_{12}$ | NA | −31.0 | −55.4 | −3.1 | −2.9 | −20.5 | 0.66 |
| $NapA_S(H_2O)_{12}$ | SMD | −28.7 | −54.8 | −5.4 | −1.5 | −20.6 | 0.72 |
| $NapA_S(H_2O)_{12}$ | IEFPCM | −30.9 | −57.3 | −3.3 | −3.4 | −21.3 | 0.69 |
| Average* | | −30.8 | −54.4 | −2.4 | −3.7 | −20.2 | 0.66 |
| Stdv | | 2.3 | 2.8 | 1.6 | 1.4 | 0.9 | 0.04 |
| Preferred value** | | −32.4 ±1.8 | | | | −20.9 ±0.4 | 0.65 ±0.05 |

* The "Average" data are the mean values of all models, and the "Stdv" data are the standard deviation of all models;
** The "preferred value" is the average results of four explicit $NO_3^-$-$NapA_S(H_2O)_n$ models with IEFPCM implicit solvent effect.

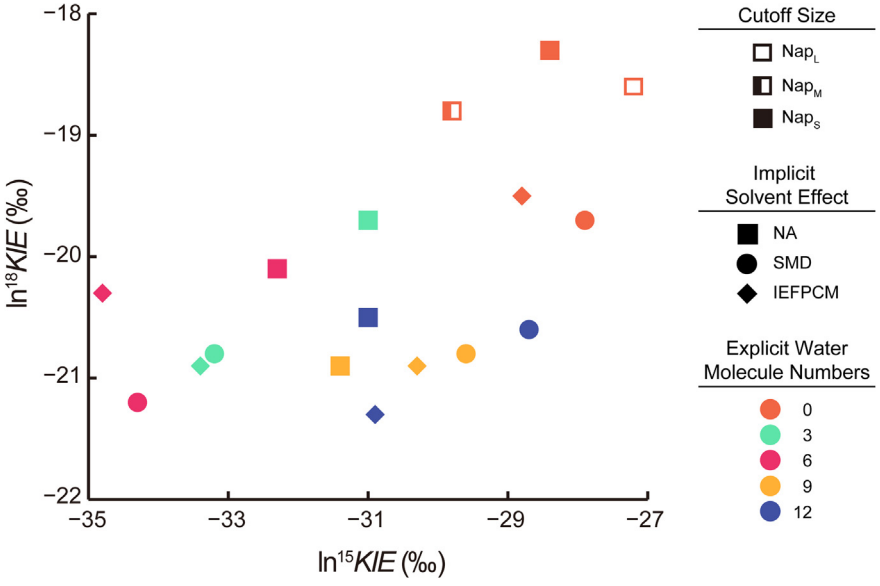


Fig. 5. Comparison of calculated ln*KIE* (‰) values of $NO_3^-$ reduction by NapA at 25 °C by models with different cutoff sizes, implicit, and explicit solvent effects.

Compare to individual $\beta$ values, the variation of KIE values introduced by implicit solvent effects are largely canceled. For the same explicit solvent models, SMD implicit solvent effect introduces maximum KIE value variations of 2.2‰ on $^{15}N$ and 1.4‰ on $^{18}O_{ave}$; IEFPCM implicit solvent effect introduces maximum KIE value variations of 2.5‰ on $^{15}N$ and 1.2‰ on $^{18}O_{ave}$. For models with the same explicit water molecule numbers, SMD and IEFPCM have a similar influence on the calculated KIE values, with maximum differences of 0.9‰ on $^{15}N$ and 1.1‰ on $^{18}O_{ave}$.

For models with or without the same implicit solvent effect, adding explicit water molecules introduce maximum KIE value variations of 3.9‰ on $^{15}N$ and 2.5‰ on $^{18}O_{ave}$. The four explicit solvent models without implicit solvent effect have maximum variations of 1.3‰ on $^{15}N$ and 1.1‰ on $^{18}O_{ave}$. However, the four explicit solvent models with SMD implicit solvent effect have maximum variations of 5.6‰ on $^{15}N$ and 0.7‰ on $^{18}O_{ave}$. The four explicit solvent models with IEFPCM implicit solvent effect have maximum differences of 4.5‰ for $^{15}N$ and 1.1‰ for $^{18}O_{ave}$. Therefore, those results indicating that solvent effects must be considered for KIE calculation of enzymatic reactions.

## 4. DISCUSSIONS AND IMPLICATIONS

### 4.1. KIE calculation setups

#### *4.1.1. Cutoff size*

For the $NapA_L$, $NapA_M$, and $NapA_S$ models without implicit nor explicit solvent effect, the calculated ln*KIE* values range from −27.2 to −29.8‰ for $^{15}N$ and from −18.3 to −18.9‰ for $^{18}O_{ave}$. Previous studies showed that, for minerals or organic molecules, only the proximal three bonds have considerable influences on the vibrational frequencies of a target atom (Liu and Tossell, 2005; Rustad et al., 2008, 2010; Li and Liu, 2011, 2015; Zhang and Liu, 2014; He and Liu, 2015; Gao et al., 2018; He et al., 2020a). The comparison between the $NapA_L$, $NapA_M$, and $NapA_S$ models showed that the KIE value differences can be as large as 2.6‰ for $^{15}N$ and 4.4‰ for $^{18}O_a$. Unlike minerals, an enzyme center with carbon chains is more flexible. Therefore, the enzyme cutoff sizes will have influences on the local configurations of the active positions. The hydrogens on the distant atoms can also have influences on the local configurations of active positions similar to the explicit solvent effect. Due to higher degrees of freedom in larger enzyme cutoff size, the transition state will be more difficult to be located. Larger enzyme cutoff size is not only time-consuming but also can easily cause convergence failure. During our calculation, we found that the C═O bond on the Cys group (Figs. 1 and 3) caused energy fluctuation that lead to convergence failure. Compare to the calculated ln*KIE* values, the variation caused by cutoff size is within 10%. Therefore, a cutoff size with the proximal three bonds can still be considered to represent the bonding environment of an enzymatic reaction and used for obtaining reasonable ln*KIE* values.

#### *4.1.2. Implicit solvent effect*

The implicit solvent effects have a relatively large influence on the optimized structures and absolute $\beta$ values of both reactant and transition states. For instance, for the $NO_3^-$-$NapA_S$ models without explicit water molecules, compare to the gas-state model, the differences in d(Mo—$O_a$) are 0.25 Å for the SMD model and 0.07 Å for the IEFPCM model. Such a variation disappears when the explicit solvent molecule reaches 12, with d(Mo—$O_a$) difference of 0.01 Å for both SMD and IEFPCM models. The influences of implicit solvent effects on the optimized reactant and transition state structures as well as the calculate $\beta$ values are largely canceled when the ln*KIE* values are reported. It is noteworthy that the influences of the implicit solvent effect are gradually decreasing with the increasing numbers of explicit water molecules. For instance, the calculated KIE value differences between $NapA_S(H_2O)_3$ models with or without the IEFPCM solvent effect is 2.4‰ for $^{15}N$ and 1.2‰ for $^{18}O_{ave}$. Such differences become −0.1‰ for $^{15}N$ and 0.8‰ for $^{18}O_{ave}$ between the $NapA_S(H_2O)_{12}$ models with or without the IEFPCM solvent effect. This result is consistent with previous studies that implicit solvent effect becomes less significant for energy calculation when a system involves more water molecules (Sevastik and Himo, 2007; Hopmann and Himo, 2008; Georgieva and Himo, 2010; Liao et al., 2011, 2015).

Based on the current data, we cannot evaluate the accuracy of the absolute $\beta$ values. Previous researches showed that the explicit-plus-implicit solvent method can provide more accurate calculation results (Gao et al., 2018). Thus, considering the implicit solvent effect is necessary. However, we have observed that adding SMD can easily introduce a small imaginary frequency. Thus, we recommend using IEFPCM implicit solvent effect. If adding implicit solvent effect caused convergence failure, the calculation of an enzymatic model only incorporates the explicit solvent effect that can provide KIE values with acceptable error.

#### *4.1.3. Explicit solvent effect*

Except for the influences on local configurations, compared to the cutoff size and implicit solvent effect, the explicit solvent effect can also significantly affect the calculated ln*KIE* values from about −28‰ to −31‰ for $^{15}N$, and from −19‰ to −20‰ for $^{18}O_{ave}$. Therefore, to estimate the KIE values of an enzymatic reaction, the explicit solvent effect must be considered. In real enzymatic reactions, the solvent molecules are not only water but also protein. Nevertheless, the solvent molecules only form hydrogen bonds with the reactant. Water molecules serve a similar purpose to protein molecules. For example, the calculation of catalytic cis-Dihydroxylation of nitrobenzene and 2-nitrotoluene showed that incorporating different amino acid residues or water molecules to the reaction system produced similar transition state structures (Pabis et al., 2014). Thus, surrounding an active center of an enzymatic reaction with only water molecules should properly simulate the reaction environment. One additional reason that protein pieces substrates are not recommended is that protein pieces have more atoms and more complex structures than water molecules, which consumes extra computational times and can easily cause convergence failure.

Due to the local configuration variations caused by explicit solvent molecules, sampling multiple configurations

are necessary. A $\beta$ value of a compound in aqueous phase usually converges at the models with 24–36 water molecules (Zhang and Liu, 2014; He and Liu, 2015; Gao et al., 2018). However, for the nitrate reduction models with 3, 6, 9, and 12 water molecules in this study, we find that increasing the numbers of water molecules does not significantly affect the calculated KIE values. A reactant, which binds with an enzyme, leaves only half of its surrounding space open. Therefore, the influence of the explicit solvent effect is smaller on the calculated KIE value of an enzymatic reaction than a $\beta$ value of a compound in the aqueous phase. The 1‰ variation observed in our calculation will be averaged out by sampling multiple configurations. Thus, for an enzymatic reaction, sampling multiple configurations of models with 12 to 18 explicit water molecules would produce more accurate KIE values.

Here, we report the average value of the four IEFPCM-plus-explicit solvent models as the preferred calculated KIE values of nitrate reduction by NapA, which are $\ln^{15}KIE = -32.4 \pm 1.8$ ‰ and $\ln^{18}KIE = -20.9 \pm 0.4$ ‰ with $\ln^{18}KIE$: $\ln^{15}KIE = 0.65 \pm 0.05$. It should be noted that our calculations only consider the N—O bond-breaking step. As discussed above, $\alpha_{NapA}$ also involves the EIE among $NO_3^-$ in the aqueous phase and $NO_3^-$-enzyme complex ($EIE = \beta_{NO_3^- - NapA}/\beta_{NO_3^-(aq)}$). The $\beta$ values of $NO_3^-$ in solution can be estimated by water droplet method, which has been widely used in the $\beta$ value calculation of species in aqueous phase (Rustad et al., 2008, 2010; Zhang and Liu, 2014; He and Liu, 2015). The calculated ln*EIE* values for both $^{15}N$ and $^{18}O_{ave}$ are in several per mils ($^{15}\beta_{NO_3^-(aq)} = 1.1577$ and $^{18}\beta_{NO_3^-(aq)} = 1.0995$: Harmonic results of IEFPCM-plus-explicit solvent models by B3LYP/6-31 + g(d,p) basis set without scaling factor). Considering the EIE among $NO_3^-$ in the aqueous phase and $NO_3^-$-enzyme complex, the isotope fractionation factors do not change in degrees, and the calculated $\ln^{18}\alpha_{NapA}$: $\ln^{15}\alpha_{NapA}$ value does not vary much compared with the calculated $^{18}\ln KIE$: $^{15}\ln KIE$ value ($\ln^{15}\alpha_{NapA} = -34.8$‰ and $\ln^{18}\alpha_{NapA} = 21.0$‰ with $\ln^{18}\alpha_{NapA}$:$\ln^{15}\alpha_{NapA} = 0.60$. Therefore, our calculation results can be compared with experimental results.

### 4.2. Bonded isotope effect of nitrate reduction

The observed stable isotope fractionation factor ($\alpha_{obs}$) in laboratory experiments or field observations may not equal to the intrinsic KIE of an elementary step since it will be affected by substrate concentration, microbial activity, commitment to catalysis, transportation through the cell membrane, the competition between microbial individuals or groups, and other mixing or mass transfer processes (Thullner et al., 2012; Treibergs and Granger, 2017; He and Bao, 2019). It leads to major uncertainties in linking an $\alpha_{obs}$ to a KIE and further deducing the fundamental reaction mechanism. In addition to a single $\alpha$ value of an element, the relationships between the $\alpha$ values of two or more elements in a compound named bonded isotope effect (BIE, He and Bao, 2019), is more conserved for a specific reaction under different conditions (Hatzinger et al., 2009; Thullner et al., 2012; He and Bao, 2019). In the study of nitrate, the nitrogen-oxygen BIE has already become one fundamental tool to identify *in situ* reaction mechanisms (Bottcher et al., 1990; Fukada et al., 2003, 2004; Lehmann et al., 2003, 2004; Granger et al., 2004; Sigman et al., 2005; Wankel et al., 2007, 2009; Itoh et al., 2011; Casciotti et al., 2013; Wankel et al., 2015; Granger and Wankel, 2016; Buchwald et al., 2018).

To better understand the reaction mechanism of nitrate reduction, laboratory experiments had been implemented to calibrate KIEs and BIEs of nitrate reduction processes (Granger et al., 2008; Karsh et al., 2012; Carlisle et al., 2014; Frey et al., 2014; Treibergs and Granger, 2017). The KIE reported in the abovementioned literature uses the definition of $\varepsilon = {}^{light}k/{}^{heavy}k - 1 = 1/(\alpha - 1)$. Here we convert all values to ln$\alpha$. Under different experimental conditions, the observed $\ln^{15}\alpha$ and $\ln^{18}\alpha$ ranged from −6‰ to −40‰ and −6‰ to −32‰, respectively. However, the $\ln^{18}\alpha$: $\ln^{15}\alpha$ value showed a binomial distribution, either around 1 (0.86–1.17, Granger et al., 2008; Karsh et al., 2012; Treibergs and Granger, 2017), or around 0.6 (0.46–0.68, Granger et al., 2008; Frey et al., 2014; Treibergs and Granger, 2017).

The ln$\alpha$ and $\ln^{18}\alpha$: $\ln^{15}\alpha$ values obtained from *Rhodobacter sphaeroides* NapA laboratory experiments are listed in Table 7. Two types of $NO_3^-$ reduction laboratory experiments were implemented: by bacterial strains (Granger et al., 2008) and by extracted reductase assays (Treibergs and Granger, 2017). The bacterial strain experiments obtained $\ln^{15}\alpha$ and $\ln^{18}\alpha$ values of −12.5‰ to −19.7 ‰ and −7.9‰ to −13.0‰, respectively, with $\ln^{18}\alpha$: $\ln^{15}\alpha$ values from 0.56 to 0.66 (Granger et al., 2008). The reductase assay experiments obtained $\ln^{15}\alpha$ and $\ln^{18}\alpha$ values of −36.7‰ to −39.0‰ and −18.5‰ to −19.7‰, respectively, with $\ln^{18}\alpha$: $\ln^{15}\alpha = 0.50$ (Treibergs and Granger, 2017).

Comparing with nitrate reduction experiments by bacteria, the nitrate reduction by reductase assays experiences fewer transportation processes, such as the transportation of nitrate through a membrane. It is expected that the isotope fractionation factors obtained from reductase assay experiments should be closer to the intrinsic KIE values. Our calculated results of $\ln^{15}KIE = -32.4 \pm 1.8$ ‰ and $^{18}\ln KIE = -20.9 \pm 0.4$ ‰ (Fig. 6 and Table 6) agree with the ln$\alpha$ values obtained from reductase assay experiments (Treibergs and Granger, 2017), which support the argument.

Our calculated $\ln^{18}KIE/\ln^{15}KIE$ value of $0.65 \pm 0.05$ located within the range of the bacterial strain experiments (from 0.56 to 0.66, Granger et al., 2008), and roughly comparable with the reductase assays experiments (0.50, Treibergs and Granger, 2017). In addition, the culture experiments of *Sulfurimonas gotlandica* that reduce nitrate by Nap also obtained $\ln^{18}\alpha$: $\ln^{15}\alpha$ values from 0.48 to 0.66 (Frey et al., 2014). Our one-step elementary reaction KIE calculation results can be independent evidence to support the laboratory experiments, and provide a profound understanding of the nitrate Nap reaction mechanism.

The previously reported calculated ln*KIE* values of nitrate reduction by eukaryotic assimilatory nitrate reductase, prokaryotic respiratory nitrate reductase, and Nap were ranging from −32.2 to −35.9‰ for $^{15}N$, and from

Table 7
Calculated ln*KIE* value (×1000‰) of this work and calibrated lnα values (×1000‰) from the literature for $NO_3^-$ reduction by *Rhodobacter sphaeroides*.

| | $\ln^{15}\alpha$[1] | $\ln^{18}\alpha$ | $\ln^{18}\alpha$: $\ln^{15}\alpha$ | References |
|---|---|---|---|---|
| DFT calculation[2] | −32.4 ± 1.8 | −20.9 ± 0.4 | 0.65 ± 0.05 | This work |
| Reductase assays | −36.7 ± 4.4 | −18.5 ± 2.0 | 0.50 ± 0.01 | (Treibergs and Granger, 2017)[3] |
| Reductase assays | −39.0 ± 5.4 | −19.7 ± 2.5 | 0.50 ± 0.01 | |
| Bacterial strains | −12.5 ± 0.2 | −7.9 ± 0.4 | 0.63 ± 0.02 | (Granger et al., 2008)[3] |
| Bacterial strains | −13.6 ± 0.2 | −8.6 ± 0.1 | 0.63 ± 0.01 | |
| Bacterial strains | −14.6 ± 0.3 | −8.7 ± 1.0 | 0.59 ± 0.02 | |
| Bacterial strains | −14.4 ± 0.1 | −8.6 ± 0.3 | 0.59 ± 0.02 | |
| Bacterial strains | −17.9 ± 0.2 | −10.2 ± 0.2 | 0.57 ± 0.02 | |
| Bacterial strains | −15.9 ± 0.2 | −8.9 ± 0.1 | 0.56 ± 0.00 | |
| Bacterial strains | −15.6 ± 0.4 | −9.5 ± 0.1 | 0.61 ± 0.00 | |
| Bacterial strains | −14.7 ± 2.8 | −9.7 ± 2.8 | 0.66 ± 0.04 | |
| Bacterial strains | −15.8 ± 0.2 | −8.9 ± 0.2 | 0.56 ± 0.03 | |
| Bacterial strains | −19.7 ± 0.2 | −13.0 ± 0.2 | 0.66 ± 0.06 | |

Note: 1. The definition of ε in literature is $^{light}k/^{heavy}k-1 = 1/(\alpha-1)$. Here we convert all the values to lnα values.
2. For the DFT calculation, the reported lnα values are ln*KIE*, and the reported $\ln^{18}\alpha$: $\ln^{15}\alpha$ values are $\ln^{18}KIE/\ln^{15}KIE$.
3. See references for the experimental conditions.

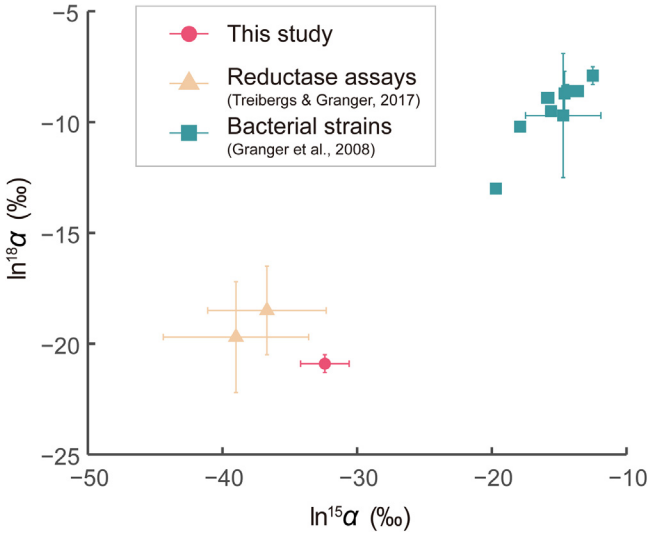


Fig. 6. Calculated ln*KIE* or calibrated lnα values (‰) for $NO_3^-$ reduction by *Rhodobacter sphaeroides* of this work (pink circle), reductase assay experiments (yellow triangles, Treibergs and Granger, 2017), and bacterial strain experiments (green squares, Granger et al., 2008). (For interpretation of the references to colour in this figure legend, the reader is referred to the web version of this article.)

−33.0 to −34.2‰ for $^{18}O$ with $\ln^{18}KIE/\ln^{15}KIE$ values from 0.9 to 1.1 (Guo et al., 2010). Our calculation shows similar $\ln^{15}KIE$ values, but distinctive $\ln^{18}KIE$ values. However, its computational details were not given. Thus, we cannot evaluate the results, nor discuss the reaction mechanism differences.

## 5. CONCLUSIONS

We have built 17 models to test the influences of cutoff size and solvent effects on KIE calculation of $NO_3^-$ reduction by the active center of *Rhodobacter sphaeroides* NapA under DFT B3LYP/6-31+g(d,p) level. The calculation results show that to estimate the KIE value of an enzymatic reaction, we can simplify the system of interest to a cutoff model with the proximal three bonds to the active position. The implicit solvent effect has a limited influence on the calculated KIE values when explicit solvent molecules are involved. Sampling multiple configurations using explicit solvent models with 12 to 18 water molecules are necessary for accurate prediction of KIE values. The transition state of $NO_3^-$ reduction by NapA has Mo—$O_a$ and $O_a$—N bond length of 1.90 ± 0.02 Å and 1.75 ± 0.02 Å, respectively, with the ∠Mo—$O_a$—N angle of 128.2 ± 2.9°. Using IEFPCM-plus-explicit solvent models, the obtained $\ln^{15}KIE$ and $\ln^{18}KIE$ values are −32.4 ± 1.8 ‰ and −20.9 ± 0.4‰, respectively, with $\ln^{18}KIE/\ln^{15}KIE = 0.65 \pm 0.05$. Our results are consistent with previous laboratory experiments, which support the validity of the proposed calculation settings.

## Declaration of Competing Interest

The authors declare that they have no known competing financial interests or personal relationships that could have appeared to influence the work reported in this paper.

### ACKNOWLEDGMENT

The project is benefited from discussions with C.H. Gao and L. Geng. We are grateful for the funding supports from the China Postdoctoral Science Foundation [2019M660811], the strategic priority research program (B) of CAS [XDB41000000, XDB18010100], and Chinese NSF project [41773016, 41530210].

## APPENDIX A. SUPPLEMENTARY MATERIAL

Supplementary data to this article can be found online at https://doi.org/10.1016/j.gca.2020.10.027.

### REFERENCES

Acevedo O. and Evanseck J. D. (2003) The effect of solvent on a Lewis acid catalyzed Diels-Alder reaction, using computed and experimental kinetic isotope effects. *Org. Lett.* **5**, 649–652.

Adamczyk P., Dybala-Defratyka A. and Paneth P. (2011) DFT study of trichloroethene reaction with permanganate in aqueous solution. *Environ. Sci. Technol.* **45**, 3006–3011.

Adamczyk P., Wijker R. S., Hofstetter T. B. and Paneth P. (2014) A DFT study of permanganate oxidation of toluene and its ortho-nitroderivatives. *J. Mol. Model.* **20**.

Anisimov V. and Paneth P. (1999) ISOEFF98. A program for studies of isotope effects using Hessian modifications. *J. Math. Chem.* **26**, 75–86.

Arnoux P., Sabaty M., Alric J., Frangioni B., Guigliarelli B., Adriano J. M. and Pignol D. (2003) Structural and redox plasticity in the heterodimeric periplasmic nitrate reductase. *Nat. Struct. Biol.* **10**, 928–934.

Bao H., Cao X. and Hayles J. A. (2016) Triple oxygen isotopes: fundamental relationships and applications. *Annu. Rev. Earth Planet. Sci.* **44**, 463–492.

Becke A. D. (1993) Density-functional thermochemistry. III. The role of exact exchange. *J. Chem. Phys.* **98**, 5648–5652.

Biaso F., Burlat B. and Guigliarelli B. (2012) DFT investigation of the molybdenum cofactor in periplasmic nitrate reductases: structure of the Mo(V) EPR-active species. *Inorg. Chem.* **51**, 3409–3419.

Bigeleisen J. (1949) The relative reaction velocities of isotopic molecules. *J. Chem. Phys.* **17**, 675–678.

Bigeleisen J. and Mayer M. G. (1947) Calculation of equilibrium constants for isotopic exchange reactions. *J. Chem. Phys.* **15**, 261–267.

Bigeleisen J. and Wolfsberg M. (1958) Theoretical and experimental aspects of isotope effects in chemical kinetics. *Adv. Chem. Phys.*, 15–76.

Bottcher J., Strebel O., Voerkelius S. and Schmidt H. L. (1990) Using isotope fractionation of nitrate nitrogen and nitrate oxygen for evaluation of microbial denitrification in a Sandy Aquifer. *J. Hydrol.* **114**, 413–424.

Buchwald C., Homola K., Spivack A. J., Estes E. R., Murray R. W. and Wankel S. D. (2018) Isotopic constraints on nitrogen transformation rates in the deep sedimentary marine biosphere. *Global Biogeochem. Cycles* **32**, 1688–1702.

Burton G. W., Sims L. B., Wilson J. C. and Fry A. (1977) Calculation of carbon-14, chlorine-37, and deuterium kinetic isotope effects in the solvolysis of tert-butyl chloride. *J. Am. Chem. Soc.* **99**, 3371–3379.

Carlisle E., Yarnes C., Toney M. D. and Bloom A. J. (2014) Nitrate reductase N-15 discrimination in Arabidopsis thaliana, Zea mays, Aspergillus niger, Pichea angusta, and Escherichia coli. *Front. Plant Sci.* **5**.

Casciotti K. L., Buchwald C. and McIlvin M. (2013) Implications of nitrate and nitrite isotopic measurements for the mechanisms of nitrogen cycling in the Peru oxygen deficient zone. *Deep-Sea Res Pt I* **80**, 78–93.

Cerqueira N. M. F. S. A., Gonzalez P. J., Brondino C. D., Romao M. J., Romao C. C., Moura I. and Moura J. J. G. (2009) The effect of the sixth sulfur ligand in the catalytic mechanism of periplasmic nitrate reductase. *J. Comput. Chem.* **30**, 2466–2484.

Cerqueira N. M. F. S. A., Pakhira B. and Sarkar S. (2015) Theoretical studies on mechanisms of some Mo enzymes. *J. Biol. Inorg. Chem.* **20**, 323–335.

Coelho C. and Romão M. J. (2015) Structural and mechanistic insights on nitrate reductases. *Protein Sci.* **24**, 1901–1911.

Crawford A. M., Cotelesage J. J. H., Prince R. C. and George G. N. (2019) The Catalytic Mechanisms of the Molybdenum and Tungsten Enzymes. In *Metallocofactors that Activate Small Molecules: With Focus on Bioinorganic Chemistry* (ed. M. W. Ribbe). Springer International Publishing, Cham, pp. 63–100.

Dias J. M., Than M. E., Humm A., Huber R., Bourenkov G. P., Bartunik H. D., Bursakov S., Calvete J., Caldeira J. and Carneiro C. (1999) Crystal structure of the first dissimilatory nitrate reductase at 1.9 angstrom solved by MAD methods. *Structure* **7**, 65–79.

Eyring H. (1935a) The activated complex and the absolute rate of chemical reactions. *Chem. Rev.* **17**, 65–77.

Eyring H. (1935b) The activated complex in chemical reactions. *J. Chem. Phys.* **3**, 107–115.

Felipe M. A., Xiao Y. T. and Kubicki J. D. (2001) Molecular orbital modeling and transition state theory in geochemistry. *Rev. Mineral Geochem.* **42**, 485–531.

Firestone R. S. and Schramm V. L. (2017) The transition-state structure for human MAT2A from isotope effects. *J. Am. Chem. Soc.* **139**, 13754–13760.

Frey C., Hietanen S., Jürgens K., Labrenz M. and Voss M. (2014) N and O Isotope fractionation in nitrate during chemolithoautotrophic denitrification by Sulfurimonas gotlandica. *Environ. Sci. Technol.* **48**, 13229–13237.

Frisch M. J., Pople J. A. and Binkley J. S. (1984) Self-consistent molecular orbital methods 25. Supplementary functions for Gaussian basis sets. *J. Chem. Phys.* **80**, 3265–3269.

Frisch, M.J., Trucks, G.W., Schlegel, H.B., Scuseria, G.E., Robb, M.A., Cheeseman, J.R., Scalmani, G., Barone, V., Petersson, G.A., Nakatsuji, H., Li, X., Caricato, M., Marenich, A.V., Bloino, J., Janesko, B.G., Gomperts, R., Mennucci, B., Hratchian, H.P., Ortiz, J.V., Izmaylov, A.F., Sonnenberg, J. L., Williams, Ding, F., Lipparini, F., Egidi, F., Goings, J., Peng, B., Petrone, A., Henderson, T., Ranasinghe, D., Zakrzewski, V.G., Gao, J., Rega, N., Zheng, G., Liang, W., Hada, M., Ehara, M., Toyota, K., Fukuda, R., Hasegawa, J., Ishida, M., Nakajima, T., Honda, Y., Kitao, O., Nakai, H., Vreven, T., Throssell, K., Montgomery Jr., J.A., Peralta, J.E., Ogliaro, F., Bearpark, M.J., Heyd, J.J., Brothers, E.N., Kudin, K.N., Staroverov, V.N., Keith, T.A., Kobayashi, R., Normand, J., Raghavachari, K., Rendell, A.P., Burant, J.C., Iyengar, S.S., Tomasi, J., Cossi, M., Millam, J.M., Klene, M., Adamo, C., Cammi, R., Ochterski, J.W., Martin, R.L., Morokuma, K., Farkas, O., Foresman, J.B. and Fox, D.J., 2016. Gaussian 16 Rev. B.01. 2016.

Fukada T., Hiscock K. M. and Dennis P. F. (2004) A dual-isotope approach to the nitrogen hydrochemistry of an urban aquifer. *Appl. Geochem.* **19**, 709–719.

Fukada T., Hiscock K. M., Dennis P. F. and Grischek T. (2003) A dual isotope approach to identify denitrification in groundwater at a river-bank infiltration site. *Water Res.* **37**, 3070–3078.

Galimov E. M. (2006) Phenomenon of life: between equilibrium and non-linearity. Origin and principles of evolution. *Geochem. Int.* **44**, S1–S95.

Gao C., Cao X., Liu Q., Yang Y., Zhang S., He Y., Tang M. and Liu Y. (2018) Theoretical calculation of equilibrium Mg isotope fractionations between minerals and aqueous solutions. *Chem. Geol.* **488**, 62–75.

Georgieva P. and Himo F. (2010) Quantum chemical modeling of enzymatic reactions: the case of histone lysine methyltransferase. *J. Comput. Chem.* **31**, 1707–1714.

Geronimo I. and Paneth P. (2014) A DFT and ONIOM study of C-H hydroxylation catalyzed by nitrobenzene 1,2-dioxygenase. *PCCP* **16**, 13889–13899.

Glasser N. R., Oyala P. H., Osborne T. H., Santini J. M. and Newman D. K. (2018) Structural and mechanistic analysis of the arsenate respiratory reductase provides insight into environmental arsenic transformations. *Proc. Natl. Acad. Sci. USA* **115**, E8614–E8623.

Granger J., Sigman D. M., Lehmann M. F. and Tortell P. D. (2008) Nitrogen and oxygen isotope fractionation during dissimilatory nitrate reduction by denitrifying bacteria. *Limnol. Oceanogr.* **53**, 2533–2545.

Granger J., Sigman D. M., Needoba J. A. and Harrison P. J. (2004) Coupled nitrogen and oxygen isotope fractionation of nitrate during assimilation by cultures of marine phytoplankton. *Limnol. Oceanogr.* **49**, 1763–1773.

Granger J. and Wankel S. D. (2016) Isotopic overprinting of nitrification on denitrification as a ubiquitous and unifying feature of environmental nitrogen cycling. *Proc. Natl. Acad. Sci. USA* **113**, E6391–E6400.

Guo, W., Granger, J. and Sigman, D. (2010) Nitrate isotope fractionations during biological nitrate reduction: Insights from first principles theoretical modeling, AGU Fall Meeting Abstracts.

Guo W. F., Mosenfelder J. L., Goddard W. A. and Eiler J. M. (2009) Isotopic fractionations associated with phosphoric acid digestion of carbonate minerals: insights from first-principles theoretical modeling and clumped isotope measurements. *Geochim. Cosmochim. Acta* **73**, 7203–7225.

Gwinn W. D. (1971) Normal coordinates - general theory, redundant coordinates, and general analysis using electronic computers. *J. Chem. Phys.* **55**.

Hatzinger P. B., Böhlke J. K., Sturchio N. C., Gu B., Heraty L. J. and Borden R. C. (2009) Fractionation of stable isotopes in perchlorate and nitrate during in situ biodegradation in a sandy aquifer. *Environ. Chem.* **6**, 44–52.

Hay P. J. and Wadt W. R. (1985) Ab initio effective core potentials for molecular calculations. Potentials for K to Au including the outermost core orbitals. *J. Chem. Phys.* **82**, 299–310.

He H. and Liu Y. (2015) Silicon isotope fractionation during the precipitation of quartz and the adsorption of H4SiO4 (aq) on Fe (III)-oxyhydroxide surfaces. *Chin. J. Geochem.* **34**, 459–468.

He Y. and Bao H. (2019) Predicting high-dimensional isotope relationships from diagnostic fractionation factors in systems with diffusional mass transfer. *ACS Earth Space Chem.* **3**, 120–128.

He Y., Bao H. and Liu Y. (2020a) Predicting equilibrium intramolecular isotope distribution within a large organic molecule by the cutoff calculation. *Geochim. Cosmochim. Acta* **269**, 292–302.

He Y., Cao X. and Bao H. (2020b) Ideas and perspectives: same carbon different elements – an insight into position-specific isotope patterns within a single compound. *Biogeosciences* **17**, 4785–4795.

Hille R. (1996) The mononuclear molybdenum enzymes. *Chem. Rev.* **96**, 2757–2816.

Hille R. (2002) Molybdenum and tungsten in biology. *Trends Biochem. Sci.* **27**, 360–367.

Hopmann K. H. and Himo F. (2008) Quantum chemical modeling of the dehalogenation reaction of haloalcohol dehalogenase. *J. Chem. Theory Comput.* **4**, 1129–1137.

Iron M. A. and Gropp J. (2019) Cost-effective density functional theory (DFT) calculations of equilibrium isotopic fractionation in large organic molecules. *PCCP* **21**, 17555–17570.

Itoh M., Takemon Y., Makabe A., Yoshimizu C., Kohzu A., Ohte N., Tumurskh D., Tayasu I., Yoshida N. and Nagata T. (2011) Evaluation of wastewater nitrogen transformation in a natural wetland (Ulaanbaatar, Mongolia) using dual-isotope analysis of nitrate. *Sci. Total Environ.* **409**, 1530–1538.

Jepson B. J., Mohan S., Clarke T. A., Gates A. J., Cole J. A., Butler C. S., Butt J. N., Hemmings A. M. and Richardson D. J. (2007) Spectropotentiometric and structural analysis of the periplasmic nitrate reductase from Escherichia coli. *J. Biol. Chem.* **282**, 6425–6437.

Johnston H. S. (1966) *Gas Phase Reaction Rate Theory*. The Ronald Press, New York.

Jones J. P. and Urbauer J. L. (1991) Theoretical kinetic isotope effects for the hydride transfer from formate to carbon-dioxide - a comparison of theory with experiment. *J. Comput. Chem.* **12**, 1134–1141.

Jormakka M., Richardson D., Byrne B. and Iwata S. (2004) Architecture of NarGH reveals a structural classification of Mo-bisMGD enzymes. *Structure* **12**, 95–104.

Karsh K. L., Granger J., Kritee K. and Sigman D. M. (2012) Eukaryotic assimilatory nitrate reductase fractionates N and O isotopes with a ratio near unity. *Environ. Sci. Technol.* **46**, 5727–5735.

Klajman K., Ciepielowski G., Kamiński R., Adamczyk P. and Paneth P. (2017) Resolving discrepancy between theory and experiment in 4-nitrotoluene oxidation. *J. Phys. Chem. A* **121**, 6638–6645.

Lee C., Yang W. and Parr R. G. (1988) Development of the Colle-Salvetti correlation-energy formula into a functional of the electron density. *Phys. Rev. B* **37**, 785.

Lehmann M. F., Reichert P., Bernasconi S. M., Barbieri A. and McKenzie J. A. (2003) Modelling nitrogen and oxygen isotope fractionation during denitrification in a lacustrine redox-transition zone. *Geochim. Cosmochim. Acta* **67**, 2529–2542.

Lehmann M. F., Sigman D. M. and Berelson W. M. (2004) Coupling the N-15/N-14 and O-18/O-16 of nitrate as a constraint on benthic nitrogen cycling. *Mar. Chem.* **88**, 1–20.

Li X. and Liu Y. (2011) Equilibrium Se isotope fractionation parameters: a first-principles study. *Earth Planet. Sci. Lett.* **304**, 113–120.

Li X. and Liu Y. (2015) A theoretical model of isotopic fractionation by thermal diffusion and its implementation on silicate melts. *Geochim. Cosmochim. Acta* **154**, 18–27.

Liao R.-Z. and Siegbahn P. E. M. (2015) Mechanism and selectivity of the dinuclear iron benzoyl-coenzyme A epoxidase BoxB. *Chem. Sci.* **6**, 2754–2764.

Liao R.-Z., Yu J.-G. and Himo F. (2011) Tungsten-dependent formaldehyde ferredoxin oxidoreductase: reaction mechanism from quantum chemical calculations. *J. Inorg. Biochem.* **105**, 927–936.

Liu Y. and Tossell J. A. (2005) Ab initio molecular orbital calculations for boron isotope fractionations on boric acids and borates. *Geochim. Cosmochim. Acta* **69**, 3995–4006.

Lv P.-L., Shi L.-D., Dong Q.-Y., Rittmann B. and Zhao H.-P. (2020) How nitrate affects perchlorate reduction in a methane-based biofilm batch reactor. *Water Res.* **171** 115397.

Marenich A. V., Cramer C. J. and Truhlar D. G. (2009) Universal solvation model based on solute electron density and on a continuum model of the solvent defined by the bulk dielectric constant and atomic surface tensions. *J. Phys. Chem. B* **113**, 6378–6396.

Méheut M., Lazzeri M., Blan E. and Mauri F. (2007) Equilibrium isotopic fractionation in the kaolinite, quartz, water system: Prediction from first-principles density-functional theory. *Geochim. Cosmochim. Acta* **71**, 3170–3181.

Niks D. and Hille R. (2019) Molybdenum- and tungsten-containing formate dehydrogenases and formylmethanofuran dehydrogenases: structure, mechanism, and cofactor insertion. *Protein Sci.* **28**, 111–122.

Pabis A., Geronimo I. and Paneth P. (2014) A DFT Study of the cis-dihydroxylation of nitroaromatic compounds catalyzed by nitrobenzene dioxygenase. *J. Phys. Chem. B* **118**, 3245–3256.

Richardson D. J., Berks B. C., Russell D. A., Spiro S. and Taylor C. J. (2001) Functional, biochemical and genetic diversity of prokaryotic nitrate reductases. *Cell. Mol. Life Sci.* **58**, 165–178.

Rivard B. S., Rogers M. S., Marell D. J., Neibergall M. B., Chakrabarty S., Cramer C. J. and Lipscomb J. D. (2015) Rate-determining attack on substrate precedes rieske cluster oxidation during cis-dihydroxylation by benzoate dioxygenase. *Biochemistry* **54**, 4652–4664.

Rodgers J., Femec D. A. and Schowen R. L. (1982) Isotopic mapping of transition-state structural features associated with enzymic catalysis of methyl transfer. *J. Am. Chem. Soc.* **104**, 3263–3268.

Rustad J. R., Casey W. H., Yin Q.-Z., Bylaska E. J., Felmy A. R., Bogatko S. A., Jackson V. E. and Dixon D. A. (2010) Isotopic fractionation of Mg2+(aq), Ca2+(aq), and Fe2+(aq) with carbonate minerals. *Geochim. Cosmochim. Acta* **74**, 6301–6323.

Rustad J. R., Nelmes S. L., Jackson V. E. and Dixon D. A. (2008) Quantum-chemical calculations of carbon-isotope fractionation in CO2 (g), aqueous carbonate species, and carbonate minerals. *J. Phys. Chem. A* **112**, 542–555.

Saunders M., Laidig K. E. and Wolfsberg M. (1989) Theoretical calculation of equilibrium isotope effects using ab initio force constants: application to NMR isotope perturbation studies. *J. Am. Chem. Soc.* **111**, 8989–8994.

Schauble E., Ghosh P. and Eiler J. M. (2006) Preferential formation of 13C–18O bonds in carbonate minerals, estimated using first-principles lattice dynamics. *Geochim. Cosmochim. Acta* **70**, 2510–2529.

Scalmani G. and Frisch M. J. (2010) Continuous surface charge polarizable continuum models of solvation. I. General formalism. *J. Chem. Phys.* **132**.

Schlegel H. B. (1982) Optimization of equilibrium geometries and transition structures. *J. Comput. Chem.* **3**, 214–218.

Sevastik R. and Himo F. (2007) Quantum chemical modeling of enzymatic reactions: the case of 4-oxalocrotonate tautomerase. *Bioorg. Chem.* **35**, 444–457.

Sigman D. M., Granger J., Difiore P. J., Lehmann M. M., Ho R., Cane G. and van Geen A. (2005) Coupled nitrogen and oxygen isotope measurements of nitrate along the eastern North Pacific margin. *Global Biogeochem. Cycles* **19**.

Sims, L., Burton, G. and Lewis, D. (1977) BEBOVIB-IV: A Program for Calculating Isotope Effects in Chemical Reactions. Department of Chemistry, Indiana University.

Sparacino-Watkins C., Stolz J. F. and Basu P. (2014) Nitrate and periplasmic nitrate reductases. *Chem. Soc. Rev.* **43**, 676–706.

Stern M. J. and Wolfsberg M. (1966) Simplified procedure for the theoretical calculation of isotope effects involving large molecules. *J. Chem. Phys.* **45**, 4105–4124.

Tejada-Jimenez M., Chamizo-Ampudia A., Calatrava V., Galvan A., Fernandez E. and Llamas A. (2018) From the eukaryotic molybdenum cofactor biosynthesis to the moonlighting enzyme mARC. *Molecules* **23**, 3287.

Thullner M., Centler F., Richnow H.-H. and Fischer A. (2012) Quantification of organic pollutant degradation in contaminated aquifers using compound specific stable isotope analysis - review of recent developments. *Org. Geochem.* **42**, 1440–1460.

Treibergs L. A. and Granger J. (2017) Enzyme level N and O isotope effects of assimilatory and dissimilatory nitrate reduction. *Limnol. Oceanogr.* **62**, 272–288.

Turányi T. and Tomlin A. S. (2014) *Analysis of Kinetic Reaction Mechanisms*. Springer.

Urey H. C. (1947) The thermodynamic properties of isotopic substances. *J. Chem. Soc. (Resumed)*, 562–581.

Wadt W. R. and Hay P. J. (1985) Ab initio effective core potentials for molecular calculations. Potentials for main group elements Na to Bi. *J. Chem. Phys.* **82**, 284–298.

Wankel S. D., Buchwald C., Ziebis W., Wenk C. B. and Lehmann M. F. (2015) Nitrogen cycling in the deep sedimentary biosphere: nitrate isotopes in porewaters underlying the oligotrophic North Atlantic. *Biogeosciences* **12**, 7483–7502.

Wankel S. D., Kendall C. and Paytan A. (2009) Using nitrate dual isotopic composition (delta N-15 and delta O-18) as a tool for exploring sources and cycling of nitrate in an estuarine system: Elkhorn Slough, California. *J. Geophys. Res.: Biogeosciences* **114**.

Wankel S. D., Kendall C., Pennington J. T., Chavez F. P. and Paytan A. (2007) Nitrification in the euphotic zone as evidenced by nitrate dual isotopic composition: observations from Monterey Bay, California. *Global Biogeochem. Cycles* **21**.

Wei W.-J., Siegbahn P. E. M. and Liao R.-Z. (2017) Theoretical Study of the Mechanism of the Nonheme Iron Enzyme EgtB. *Inorg. Chem.* **56**, 3589–3599.

Weinberg D. R., Gagliardi C. J., Hull J. F., Murphy C. F., Kent C. A., Westlake B. C., Paul A., Ess D. H., McCafferty D. G. and Meyer T. J. (2012) Proton-coupled electron transfer. *Chem. Rev.* **112**, 4016–4093.

Wiest O., Black K. A. and Houk K. N. (1994) Density functional theory isotope effects and activation energies for the Cope and Claisen rearrangements. *J. Am. Chem. Soc.* **116**, 10336–10337.

Williams I. H. (2012) Kinetic isotope effects from QM/MM subset hessians: "Cut-Off" analysis for SN2 methyl transfer in solution. *J. Chem. Theory Comput.* **8**, 542–553.

Williams I. H. and Wilson P. B. (2016) Kinetic isotope effects. In *Simulating Enzyme Reactivity: Computational Methods in Enzyme Catalysis* (eds. I. Tuñón and V. Moliner). Royal Society of Chemistry, pp. 150–184.

Wolfsberg M. and Stern M. (1964) Validity of some approximation procedures used in the theoretical calculation of isotope effects. *Pure Appl. Chem.* **8**, 225–242.

Wong K. Y., Xu Y. Q. and Xu L. (2015) Review of computer simulations of isotope effects on biochemical reactions: from the Bigeleisen equation to Feynman's path integral. *Bba-Proteins Proteom.* **1854**, 1782–1794.

Wujec M. and Paneth P. (2007) Mechanism of 4-methyl-1,2,4-triazol-3-thiole reaction with formaldehyde. A DFT study. *J. Phys. Org. Chem.* **20**, 1043–1049.

Yamazaki C., Kashiwa S., Horiuchi A., Kasahara Y., Yamamura S. and Amachi S. (2020) A novel dimethylsulfoxide reductase

family of molybdenum enzyme, Idr, is involved in iodate respiration by Pseudomonas sp. *SCT. Environ. Microbiol.* **22**, 2196–2212.

Youngblut M. D., Tsai C. L., Clark I. C., Carlson H. K., Maglaqui A. P., Gau-Pan P. S., Redford S. A., Wong A., Tainer J. A. and Coates J. D. (2016) Perchlorate reductase is distinguished by active site aromatic gate residues. *J. Biol. Chem.* **291**, 9190–9202.

Zeebe R. E. (2014) Kinetic fractionation of carbon and oxygen isotopes during hydration of carbon dioxide. *Geochim. Cosmochim. Acta* **139**, 540–552.

Zhang S., Liu Q., Tang M. and Liu Y. (2020) Molecular-level mechanism of phosphoric acid digestion of carbonates and recalibration of the 13C–18O clumped isotope thermometer. *ACS Earth Space Chem.* **4**, 420–433.

Zhang S. T. and Liu Y. (2014) Molecular-level mechanisms of quartz dissolution under neutral and alkaline conditions in the presence of electrolytes. *Geochem. J.* **48**, 189–205.

*Associate editor:* Shuhei Ono